

Bacterial Dynamics in Curved Spaces

Cristian Villalobos Concha,¹ Maria Luisa Cordero,¹ Rodrigo Soto,¹ Anke Lindner,² Eric Clément,² Teresa Lopez-Leon,³ and Zhengyang Liu^{2,3}

¹Departamento de Física, FCFM, Universidad de Chile, Santiago, Chile.

²Laboratoire PMMH, UMR 7636 CNRS-ESPCI-Sorbonne Université-Université Paris Diderot, 7-9 quai Saint-Bernard, 75005 Paris, France.

³Laboratoire Gulliver, UMR 7083 CNRS, ESPCI Paris, PSL Research University, 75005 Paris, France.

(Dated: January 13, 2023)

The interplay between complex environments and active matter suggests a possibility to control and engineer active matter by carefully designing the confinement structures. It is now well established that confinement may influence transport, rheology, pressure, spatial distribution and collective motion of active matter. Curved confining walls, which are ubiquitous in biological systems, show their own, specific rich and intriguing effects on active matter. Here, using a double emulsion system, where the inner and outer droplet sizes can be independently controlled, we experimentally investigate the influence of curved confinement on an active bath of *Escherichia coli* (*E. coli*) bacteria. In particular, we analyze the fluctuations of the inner droplet using the framework of a stochastic “active noise” model, and show that the strength of active noise is not an intrinsic property of an active bath, but depends on the confinement curvature. Our numerical simulations revealed the origin of this dependence on confinement. Our results pose new challenge to active matter theory and suggest new methods to control active matter.

I. INTRODUCTION

The interactions between active and passive objects are always intriguing. On the one hand, passive objects are often used as a probe to assess the properties, in particular activity, which are sometimes challenging to measure directly. On the other hand, the capabilities of activity to enhance mixing of fluids and transport of nutrients show great ecological significance and can potentially enable important biomedical applications [1–4].

On the most elementary level, the interaction between an active particle and a passive particle can be described as “scattering”. In this process, the active particle swims by the passive particle results in a closed-loop trajectory, due to the hydrodynamic head-rear symmetry of the model swimmer [5]. In the presence of a confining wall, the flow field generated by an active swimmer is modified, as if there is a mirror image of the swimmer, with force singularities pointing in opposite directions [6]. The head-rear symmetry is broken in the modified flow field, leading to net displacement of passive object in a single scattering event. Based on this picture, Mino et al. successfully modeled the confinement effect on the diffusivity of passive particles in active bath [7, 8]. Lagarde *et al.* [9] focused their experiment more on the single scattering event, and found far field hydrodynamic interactions to be irrelevant compared to direct collisions. The experiments mentioned above all revealed an important aspect of active baths: the effect on passive tracer diffusivity is stochastic and additive. This discovery has led to efforts to model active baths as a stochastic noise [10–13].

Boundaries are known to have dramatic impact on active matter, with examples of pattern formation, directed flow and unusual mechanical properties [14–16]. Planar boundaries, which are common and easy to pro-

duce in labs, have been studied extensively in the past two decades. However, less is known about how curved boundaries affect active matter behavior.

In this paper, we experimentally investigate this question by putting active bacterial suspensions into the middle layer (also known as the “shell” layer) of oil-water-oil double emulsions. We analyze the fluctuations of the inner droplet using the framework of a stochastic “active noise” model, and show that the strength of active noise is not an intrinsic property of an active bath, but depends on the confinement curvature. Furthermore, we show that the dependence on confinement originates from two aspects: collision angle and activity. Our numerical simulations reveal the origin how spherical confining wall reduces the activity of an active bath. Our results deepen the understanding of active matter behavior under confinement.

II. EXPERIMENT

A. Bacterial culture

Wild-type *E. coli* bacteria (strain W3110) were grown with a standard culturing protocol [17]. 10 μ l of frozen stock stored at -20°C was diluted in 10 ml of lysogenic broth (LB) and incubated overnight in a shaking incubator at temperature 30°C and 210 rpm. The overnight culture was then diluted in 100 times in LB and let grow for 3.5 hours to reach the optical density at 600 nm (OD) of 0.6 ± 0.1 . Bacteria were harvested by centrifuging the suspensions at 2100 g for 10 min. Then the supernatant was removed, and the pellet was resuspended in a minimal motility buffer, MMA (10 mM potassium phosphate, 0.1 mM EDTA and 10 mM sodium lactate [18]). In the droplet experiments, I used the MB described in Eric’s

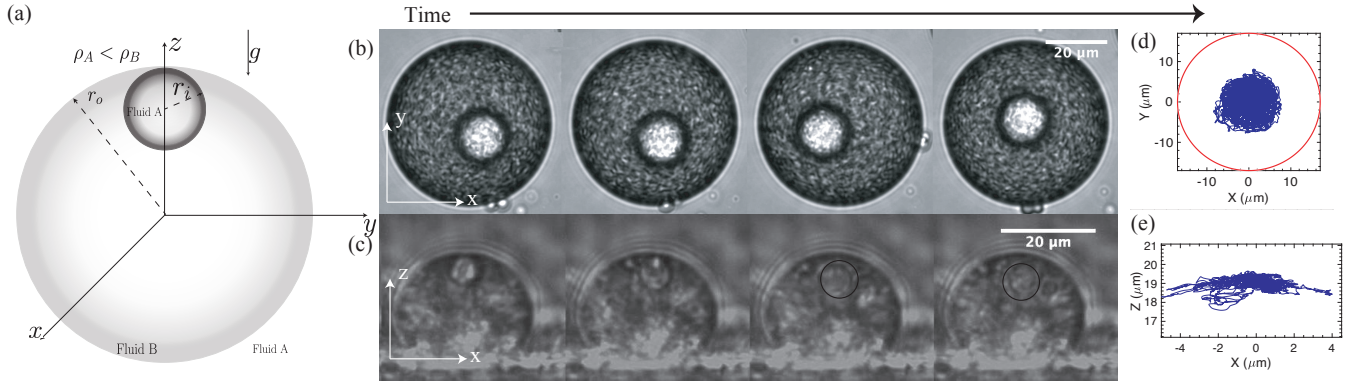


FIG. 1. **Double emulsion — bacterial shells.** (a) A Schematic diagram of the bacterial shell system, along with the coordinate system defined on it. The outer droplet of density ρ_A and radius r_o filled with bacterial suspensions. Inside this droplet there is another droplet filled with an oil of density $\rho_B < \rho_A$. (b) Sequence of image separated by $\Delta t = 5$ s. Top row; shows the XY plane of a bacterial shell of outer diameter $r_o = 27 \mu\text{m}$ and a inner droplet of diameter $r_i = 13.5 \mu\text{m}$. (c) A view of the XZ plane of a drop of diameter $r_o = 11.5 \mu\text{m}$ and a inner drop of $r_i = 2.9 \mu\text{m}$. (d-e) Trajectory of the center of the inner droplet.

protocol. The most nominal difference is the addition of L-serine. In MMA, bacteria are allowed to swim, but not to divide. The final concentration of the bacterial suspensions ranges from $OD = 0.7$ to $OD = 100$.

B. Double emulsion

Double emulsions were produced by mechanical mixing of the aqueous bacterial suspension and hexadecane (Sigma-Aldrich, H6703). 10 μl bacterial suspension was added to 1 ml hexadecane containing 2 wt% Span 80 (Sigma-Aldrich, S6760) as a surfactant. 1 wt% polyvinyl alcohol (PVA, M_w 13,000-23,000, Sigma-Aldrich, 363170) was supplemented to the oil phase to stabilize the inner droplets. The mixture is manually agitated to form many aqueous droplets in oil, among which 10% are with another oil droplet inside. Since this is an emulsion inside another emulsion, we term this experimental system a double emulsion, which is illustrated in Fig. 1(a). The double emulsion was then diluted 1:10 in hexadecane for observation. This dilution ensured enough space between droplets, so that hydrodynamic interactions can be neglected.

C. Microscopy

The same photoprinted square observation chamber was used in this work (described in Ramos *et al.* [19]). The chamber was loaded with 200 μl of the double emulsion and subsequently sealed with a coverslip to minimize evaporation. Due to density mismatch between water and hexadecane, the aqueous droplets sedimented to the bottom of the chamber, while the inner oil droplets floated to the top of the aqueous droplets. The chamber

was then placed on an inverted microscope (Nikon Ti-XX) and the double emulsions were filmed with XX camera at 50-70 Hz. The xz -plane observation was achieved by a microscope sitting on a rotating “cradle” (described in XX). Magnifications ranging from 20X to 60X were used in our experiments, depending on the size of the droplets. Figures 1(b) and (c) show some snapshots of xy -plane and xz -plane videos, respectively.

D. Image analysis

Droplet tracking was done with a method based on Hough Transform (HT), a common technique for feature extraction [20]. The results were refined by a custom Python code, which will be discussed in the appendix. Particle image velocimetry (PIV) was performed using OpenPIV package in Python [21], for characterizing bacterial activity in droplets.

III. RESULTS

A. Inner droplet trajectories

In the double emulsion experimental system, the inner droplet is frequently “kicked” by the many swimming bacteria around it. As a result, it exhibits fluctuations much stronger than Brownian motion in the horizontal (y) direction. Due to the smaller density of the inner droplet relative to the bacterial suspension, a buoyant force is constantly pushing it to the top surface of the outer droplet, making the dome an equilibrium position. In the vertical (z) direction, the inner droplet mostly follows the outer droplet surface. A typical inner droplet trajectory is shown in Fig. 2(a). The colored dots denote

the positions of inner droplet center at different time. In cases where inner droplet size is very small, while the bacterial activity is large, inner droplet can leave the surface. We can roughly estimate the critical inner droplet radius, below which bacterial activity can overcome buoyant force. The buoyant force is $F_b = \frac{4}{3}\pi r_i^3 \Delta\rho g$, where $\Delta\rho \approx 230 \text{ kg/m}^3$ is the density difference between water and hexadecane, and $g \approx 9.8 \text{ m/s}^2$ is the gravitational acceleration. The propelling force of a single bacteria is approximated by the Stokes drag on a sphere $F_a \approx 6\pi\eta r_b V_b$, where $\eta = 0.001 \text{ Pa}\cdot\text{s}$ is water viscosity, $r_b \approx 0.5 \mu\text{m}$ is bacteria cross section radius and $V_b \approx 20 \mu\text{m/s}$ is the swimming speed of bacteria. Let $F_b = F_a$, we get a critical droplet radius $r_c \approx 2.7 \mu\text{m}$. Indeed, since we never prepared inner droplet with radius $r_i < r_c$, inner droplet leaving the surface is a rare event. However, in very concentrated bacterial suspensions, the inner droplet can leave the surface even when $r_i > r_c$. This is likely due to more frequent collision events, or collective motions.

Next, we measured the position and displacement probability distribution functions (PDF) in the horizontal direction, as shown in Figs. 2(b-d). The distribution is well fitted by a Gaussian function, shown as the red curve. According to Leptos *et al.* [22], in the presence of swimmers, the displacement PDF is characterized by a Gaussian core and exponential tails. In our data, exponential tails are also observed when $\Delta t = 0.02, 0.08, 0.14 \text{ s}$, manifesting anomalous transport [Fig. 2(c)]. Further increasing the time interval makes the exponential tails disappear. When rescaling the displacement Δy with square root of time interval $\Delta t^{1/2}$, as shown in Fig. 2(d), we notice that all the Gaussian cores of the PDF curves, except the $\Delta t = 0.02, 0.08 \text{ s}$ ones, collapse on the same master curve. The deviations of the small Δt curves from the master curve suggest that strong persistence is in play at this time scale $\tau_c \approx 0.1 \text{ s}$, rather than a random diffusive process. Finally, we measured the mean square displacement (MSD) of inner droplets in all our experiments, at various bacterial concentrations and droplet sizes, as shown in Fig. 2(e). The lag time and MSD are rescaled by τ^* and $D_A \tau^*$, respectively, which are obtained from fitting the original MSD data to the 1D model described before. An example of the fit is shown in Fig. 2(f). Typically, the MSD is characterized by a superdiffusive regime at small Δt , and a transition to saturation at large Δt . A diffusive regime can be identified in some cases, but not always. The critical Δt 's, τ and τ^* , vary with droplet sizes and possibility bacterial concentrations, which will be discussed in the following section.

B. Confinement effect

We studied the motions of inner droplets in over 100 systems of various sizes and bacterial concentration. Although the simple “mechanical mixing” technique does not provide accurate control over droplet sizes, we man-

age to explore a considerable large parameter space in detail, and to reveal the confinement effect. The explored parameter space is shown in Fig. 3(a). Since we have 3 different parameters varying at the same time, we shall select experiments where two of the parameters are fixed, in order to illustrate the effect from a single parameter. Here, we choose OD $\in (20, 40]$ (blue pentagons) and OD $\in (60, 80]$ (green squares) to illustrate low and high bacterial concentrations, respectively. To see the effect of outer droplet radius r_o , we select data where $r_i \in [5, 9] \mu\text{m}$ and plot active diffusivity D_A , persistence time τ and relaxation time τ^* as functions of r_o , as shown in Fig. 3(b). We find that D_A increases monotonically with r_o at both low and high OD. The increasing rate at high OD, characterized by the slope of $D_A \cdot r_o$ curve, is much larger than that at low OD. τ and τ^* show little to no dependence on r_o in our experiments. Similarly, to see the effect of inner droplet radius r_i , we select data where $r_o \in [30, 50] \mu\text{m}$ and plot D_A , τ and τ^* as functions of r_i , as shown in Fig. 3(c). We find that neither D_A nor τ show pronounced dependence on r_i , while τ^* decreases monotonically with r_i . Interestingly, τ^* at different OD's are quite consistent in magnitude.

C. Bacterial activity

The confinement effect on the active diffusivity may be correlated with the bacterial activity. Indeed, we frequently observed very different activity at the same bacterial concentration. In order to quantify the activity, we perform PIV analysis on the bright field images of active double emulsions and use the root mean square of the PIV velocity magnitude as a measure of activity. Formally, we obtain velocity magnitude field $\mathbf{V} = \{\mathbf{V}_i\}$ from PIV. The mean velocity \bar{V} is defined as

$$\bar{V} = \sqrt{\frac{1}{N} \sum_i^N |\mathbf{V}_i|^2}. \quad (1)$$

To suppress noise from the detection, mean velocities are measured in each pair of frames and then averaged. We fix the interrogation window size at 20 pixels throughout all the analyses, with overlap between adjacent windows at 10 pixels.

In Fig. 4, we plot \bar{V} as a function of r_o . As usual, the data are put into different groups by bacterial concentrations. In each OD bin, in particular OD $\in (20, 40]$ (blue pentagons) and OD $\in (60, 80]$ (green squares), \bar{V} increases with r_o , suggesting that droplet confinement hinders the activity of bacteria. However, from this data, it is still unclear how activity depends on OD.

At the moment, we have not finished PIV on all the videos, partially due to the less organized data analysis in the past. As a result, we see less data points in Fig. 4 compared to the parameter space plot Fig. 3(a). In addition, I did not have Cristian's raw data from Chile, so it was impossible to apply the same PIV algorithm on both

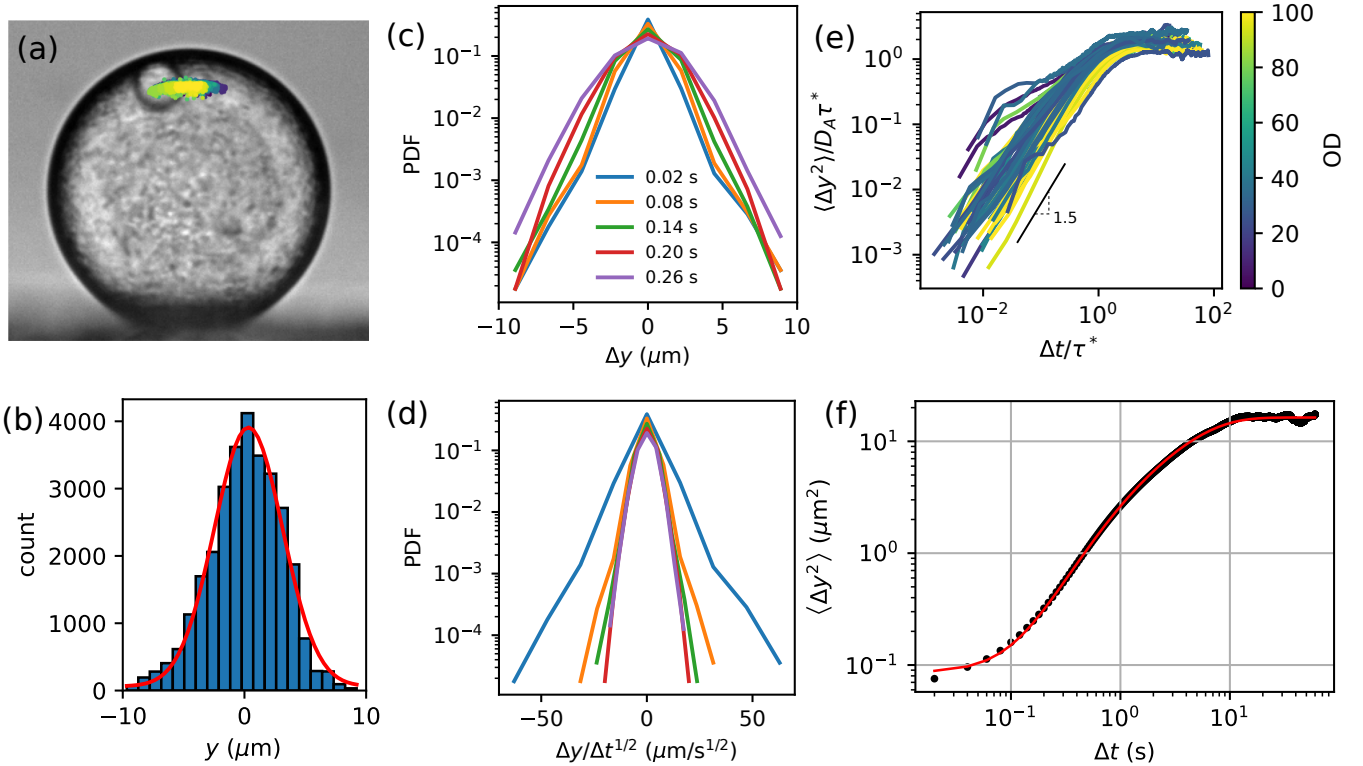


FIG. 2. Inner droplet trajectory analysis. (a) The trajectory of the inner droplet plotted on an experimental image. Outer droplet radius $r_o = 33.2 \mu\text{m}$ and inner droplet radius $r_i = 6.0 \mu\text{m}$. Color from dark purple to bright yellow denotes time from the beginning to the end. (b) Position probability distribution in y direction. Red curve is a Gaussian fit to the distribution, with mean $\mu = -0.3 \mu\text{m}$ and standard deviation $\sigma = 2.8 \mu\text{m}$. (c) Displacement probability density function (PDF) in y direction, at various time interval Δt . (d) Displacement PDF, where the displacement Δy is rescaled by the square root of time interval $\Delta t^{1/2}$. (e) Mean square displacement (MSD) of all inner droplet trajectories in this study, with time rescaled by fitted relaxation time τ^* and MSD rescaled by the product of active diffusivity and relaxation time $D_A \tau^*$. (f) A fit of MSD data to our 1D model, fitting parameters are $D_A = 1.95 \mu\text{m}^2/\text{s}$, $\tau = 0.25 \text{s}$, $\tau^* = 4.40 \text{s}$ and $c = 0.086 \mu\text{m}^2/\text{s}$.

data sets. Recently, we are transferring the raw videos from Chile to Paris. In the meantime, I am reorganizing and redoing PIV analysis on the Paris data. The goal of this reanalysis is to provide better consistency in the method. For example, when setting interrogation window size, we want the physical size (rather than pixel size) to be constant across all the analysis. There are also changes in my PIV code, related to smoothing, which can also lead to a difference in the final results. Last thing is the long standing problem regarding droplet boundary and mask, which also requires uniform treatment. In short, a REDO of PIV is ongoing, and is likely to change the results given in Fig. 4. When we have the new data, we shall discuss the interpretations and the limitations of the method, and so on.

D. Droplet lifetime

In this section, we report the time dependence of droplet activity, in particular the “frozen droplet” phenomenon. We hope to use this phenomenon as a support of our argument that confinement affects bacterial activ-

ity. However, even if this support turns out to be weak, we still can publish this phenomenon on its own, because it’s new.

It is of key importance to ensure steady state in all active matter experiment. For bacterial systems, this is particularly challenging, due to the fact that bacteria are very sensitive to their environment, which can change rapidly due to the massive metabolic activities. Our experiment typically produce 10-minute videos of active double emulsions. A typical bacterial sample used in our experiment, however, can only last around an hour, before the activity decay becomes apparent. Therefore, it is necessary to verify the steady state of experiment.

Water-in-oil emulsion has been used to confine bacteria in many previous experimental works [14, 19, 23–26]. Most of them emphasize that the videos are taken within a very short time after sample preparation, and the activity is in steady state. The claimed sample lifetimes are summarized in Table I. Being emphasized many times, steady state and sample lifetime are clearly very crucial to bacterial droplet experiments. Yet, further investigation on what determines the sample lifetime is quite rare, especially in droplet. There are two reasons: (i) previ-

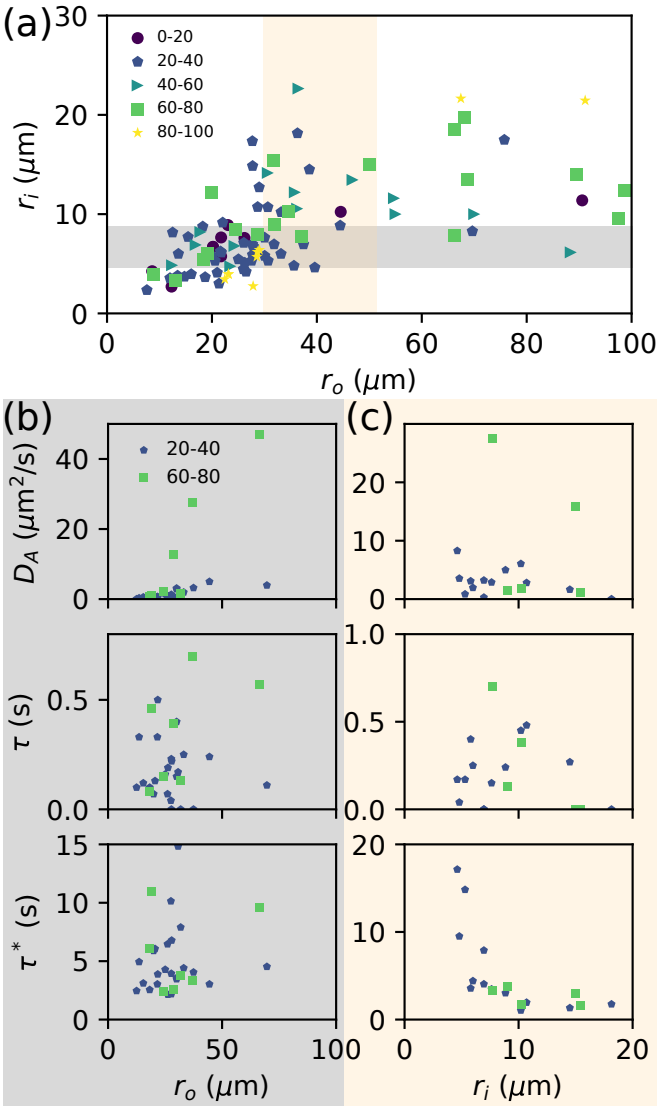


FIG. 3. Confinement effect on the inner droplet motions. (a) Explored parameter space of outer droplet radius r_o , inner droplet radius r_i and bacterial concentration in terms of optical density (OD). OD's are divided in 5 groups, shown as different colors and markers in the plot. Two bins of data are selected to highlight the confinement effect. The first bin is $r_i \in [5, 9]$ (μm), as shaded in gray. The second bin is $r_o \in [30, 50]$ (μm), as shaded in light orange. (b) Fitting parameters D_A , τ and τ^* plotted as functions of r_o in the first bin. (c) Fitting parameters D_A , τ and τ^* plotted as functions of r_i in the second bin.

ous experiment does not require very long imaging; (ii) sample lifetime can be affected by many factors, and is therefore difficult to narrow down the scope.

In this work, we perform Particle Image Velocimetry (PIV) to quantify the bacterial activity in droplets of various sizes. In Fig. 5(a), we show how mean velocity evolves over time, up to 50 minutes. Generally, the curves starts with a steady state, followed by a rapid decay. When droplets are small ($r_o < 25$ μm), it is dif-

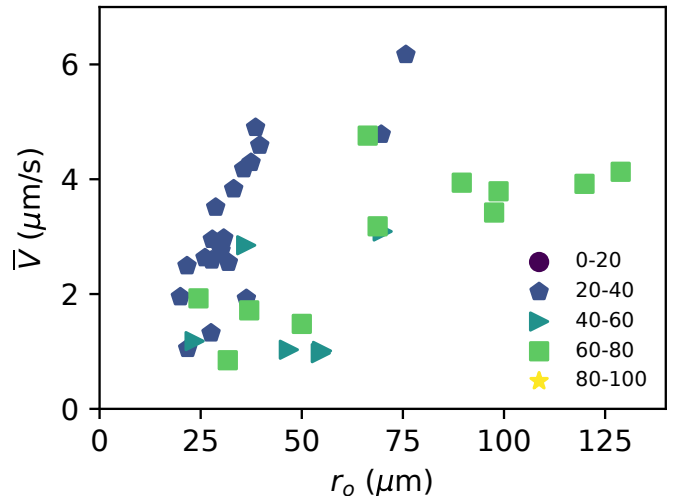


FIG. 4. Mean PIV velocity \bar{V} as a measure of bacterial activity, plotted against outer droplet radius r_o .

TABLE I. Sample lifetime in previous experiments.

Bacteria	Video time	Reference
<i>B. subtilis</i>	> 10 min	[14]
<i>E. coli</i>	3 min	[23]
<i>M. gryphiswaldense</i>	30 min	[26]
<i>E. coli</i>	30 min	[25]

ficult to identify a steady state and we always observe activity decay from the very beginning of experiments. As a result, the lifetime of bacterial droplets, which is defined as the time it takes for the mean velocity to decay to half of the initial value, depends on droplet size. In Fig. 5(b), we plot droplet lifetime as a function of droplet size. We observe that droplet lifetime generally increases with droplet size, and the time scale is on the order of 10 minutes, in agreement with previous works. It is well known that blue light generates unfavorable substances that hinders bacterial motility [27]. Therefore, we also briefly explore the effect of blue light exposure. Normally, the samples are subject to continuous light exposure, and the corresponding lifetime data are plotted in black markers in Fig. 5(b). To test the light effect, two samples are only exposed to light intermittently, and the corresponding lifetime data are plotted in red markers in Fig. 5(b). The data suggest that less exposure to blue light leads to a considerable increase of droplet lifetime. Droplet size and blue light exposure might work in a convoluted way, which is not clear so far.

E. Numerical simulation

To describe the motion of a particle of density ρ_i , radii r_i immersed in a bacterial bath with viscosity η and density ρ_0 which is confined in a spherical domain of radii r_o and density ρ_0 . We propose a Langevin equation with an

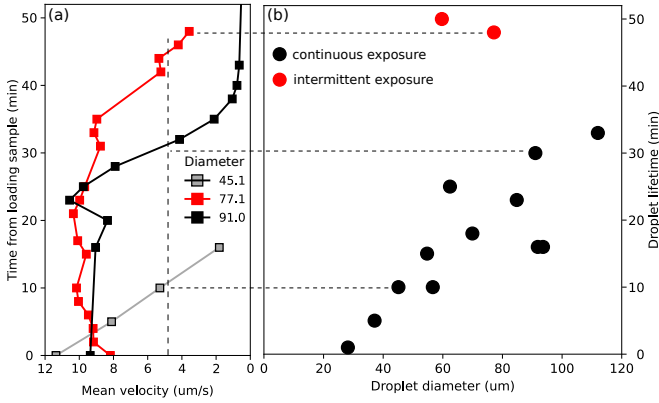


FIG. 5. (a) Mean PIV velocity \bar{V} as a measure of bacterial activity, plotted against time after loading the samples to sealed observation chambers. (b) Droplet lifetime, defined as the time it takes for the mean velocity to decay to half of the initial value, as a function of droplet diameter. The effect of light exposure is briefly explored. Continuous exposure data - the default light condition - are plotted in black markers. Intermittent exposure data, where the light is only on for 10/120 seconds, are plotted in red markers.

active noise produced by the bacterial bath and reflective boundary condition. This noise is modeled as an colored noise with zero mean. The boundary condition for the particle can be written as follow: $x^2 + y^2 + z^2 \leq (r_o - r_i)^2$, which mean that in any time t the particle is inside the sphere. The equation of motion in the limit of low Reynolds number is the following:

$$\dot{\mathbf{r}} = \mathbf{u}(t) - v_s \hat{\mathbf{z}}. \quad (2)$$

where $v_s = 2r_i^2 \Delta \rho g / 9\eta$ is the sedimentation velocity of the particle. It can be shown that a Colored noise is produced by a random motion with white noise, eg, an Uhlenbeck-Ornstein process:

$$\dot{u} = -\frac{u}{\tau} + \frac{\xi(t)}{\tau} \quad (3)$$

$$(4)$$

Where $\xi(t)$ is a white noise with zero mean and variance delta:

$$\langle \xi(t) \rangle = 0, \quad (5)$$

$$\langle \xi(t) \xi(t') \rangle = 2v_b^2 \tau \delta(t - t'). \quad (6)$$

The second moment of the velocity is:

$$\langle u(t) u(t') \rangle = v_b^2 e^{-|t-t'|/\tau}. \quad (7)$$

Which is the velocity autocorrelation function of this velocity field. To solve this system numerically, we used the Euler-Maruyama method for stochastic differential equations. As we mention before, we can produce an exponentially time correlated noise from a Ornstein-Uhlenbeck

process. Using Euler, we solve for the position of the particle and the noise for the time step n .

$$x_n = x_{n-1} + u_{x_{n-1}} dt, \quad (8)$$

$$y_n = y_{n-1} + u_{y_{n-1}} dt, \quad (9)$$

$$z_n = z_{n-1} + (u_{z_{n-1}} - v_s) dt, \quad (10)$$

$$u_n^i = u_{n-1}^i - \frac{1}{\tau} u_{n-1}^i dt + \frac{1}{\tau} v \sqrt{2\Delta t} N_n^i \quad (11)$$

Where N_n^i is a random number with zero mean and variance one.

F. One dimensional model

The confinement can be approximated to an harmonic potential, which allows us to write a one dimensional equation for the particle moving on the surface of the potential, and this can be solved analytically.

$$\dot{x} = u(t) - \frac{x}{\tilde{\tau}}. \quad (12)$$

where $\tilde{\tau} = \Gamma/k$, with Γ the friction coefficient, k the spring constant for the harmonic potential, and $u(t)$ is the active noise induced by the bacterial suspension. We will model the active noise as a colored Gaussian noise, with the following statistical properties:

$$\langle u(t) \rangle = 0, \quad (13)$$

$$\langle u(t) u(t') \rangle = v_b^2 e^{-|t-t'|/\tau}. \quad (14)$$

where v_b^2 is the intensity of the active noise, and τ is the persistence time of the bacterial fluxes. We can derive the mean-square displacement (MSD).

$$\langle \Delta x^2 \rangle = \frac{2v_b^2}{(\frac{1}{\tilde{\tau}} + \frac{1}{\tau})} \left[\frac{(1 - e^{-\frac{2}{\tilde{\tau}} t})}{\frac{2}{\tilde{\tau}}} - \frac{(e^{-(\frac{1}{\tilde{\tau}} + \frac{1}{\tau}) t} - e^{-\frac{2}{\tilde{\tau}} t})}{\frac{1}{\tilde{\tau}} - \frac{1}{\tau}} \right], \quad (15)$$

Now we can study the limits cases as: For short's times $t \rightarrow 0$:

$$\langle \Delta x^2 \rangle \approx v_b^2 t^2. \quad (16)$$

For $t \rightarrow \infty$:

$$\langle \Delta x^2 \rangle \approx \frac{v_b^2}{\frac{1}{\tau} (\frac{1}{\tilde{\tau}} + \frac{1}{\tau})}. \quad (17)$$

We can see that for short times, the MSD has a ballistic behavior, and for long times the MSD saturates.

IV. SIMULATION RESULTS

Simulation depends on four different variables r_o, r_i, v_b^2, τ . The idea here is to check under which condition the input parameters of the bath v_b, τ , remain the

same when we extract this values from the model. Equation D7 explicitly show v_b^2 and τ , but this is for the case of a point particle in the presence of the bath. So lets re-write the equation to:

$$= \frac{2v_{\text{fit}}^2}{(\frac{1}{\tilde{\tau}_{\text{fit}}} + \frac{1}{\tau_{\text{fit}}})} \left[\frac{(1 - e^{-\frac{2}{\tilde{\tau}_{\text{fit}}}t})}{\frac{2}{\tilde{\tau}_{\text{fit}}}} - \frac{(e^{-(\frac{1}{\tilde{\tau}_{\text{fit}}} + \frac{1}{\tau_{\text{fit}}})t} - e^{-\frac{2t}{\tilde{\tau}_{\text{fit}}}})}{\frac{1}{\tilde{\tau}_{\text{fit}}} - \frac{1}{\tau_{\text{fit}}}} \right]. \quad (18)$$

To fit the MSD of the particle, I used the following procedure:

- From the Slope MSD: $\alpha(t) = \frac{d(\log(\langle \Delta x^2(t) \rangle))}{d \log(t)}$ find the time when the slope is $\alpha = 1.7$.
- Fit the MSD up to t when $\alpha = 1.7$ with the MSD for an Active Brownian Particle (ABP).
- $\langle \Delta x^2 \rangle = v_b^2 [t - \tau(1 - e^{-t/\tau})]$
- Here extract v_{fit} , τ_{fit} .
- Then fit the whole MSD with v_{fit} , τ_{fit} fixed to determine $\tilde{\tau}_{\text{fit}}$

A. Effect of Change r_o

Here as we kept r_i constant, we are changing the confinement. While changing r_o we also change the value of $\tilde{\tau}$. The input parameters are: $r_i = 10\mu\text{m}$, $\tau = 1\text{s}$, $v_b = 1\mu\text{m/s}$.

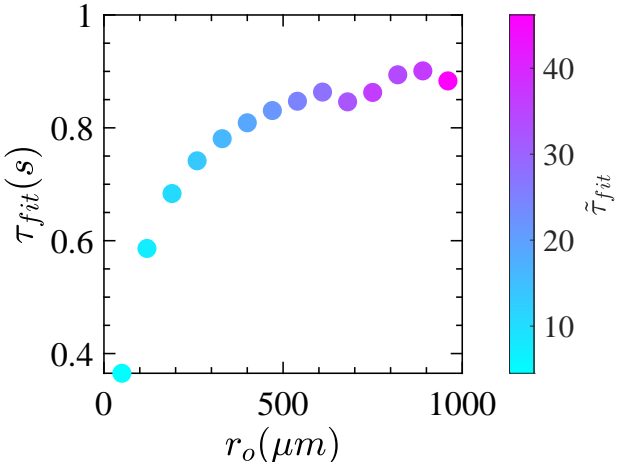


FIG. 6.

V. DISCUSSIONS

In this section, we discuss the results. For the results we understand, we can provide more insight, e.g. by giving more detailed description and analysis of a model.

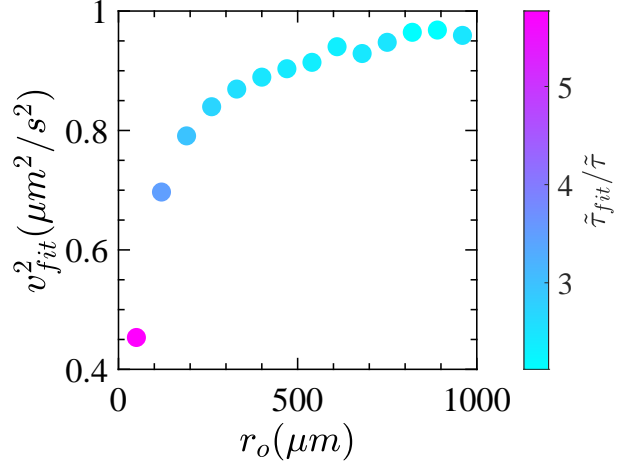


FIG. 7.

For the results we do not understand yet, we discuss in the context of literature, and pose specific open questions for future research to follow up.

Appendix A: Droplet tracking

Although the HT method can roughly detect the locations of the inner droplets, the accuracy was not satisfactory when we just use it as it was. There are two major issues: (i) No subpixel accuracy: all the detections are separated from each other by integer pixels; (ii) Inconsistent detection: whether the algorithm detects the inner edge or the outer edge of a droplet is not consistent, essentially because it only considers the pixel intensity gradient.

To resolve these issues, we build a custom correction method to refine the results by HT. In our images of droplets, we notice that all the droplets have dark edges, which may be a result of strong refraction at the edges. If we draw a line from droplet center, in the radial direction, to outside the droplet (yellow lines in Fig. 8(a)), the image intensity profile along that line would likely show a valley (a dark peak, indicated as red spots in Fig. 8(a)). This valley turns out to be a more unambiguous indicator of the droplet edge position. By drawing multiple lines across the droplet boundary and analyzing each pixel intensity profile to get a valley position, we get the coordinates of multiple points on the droplet edge, from which we can fit a circle. As shown in Fig. 8(b), the orange circle is a result of the above fitting procedure. Compare to the original detection of the HT method (blue circle in Fig. 8(b)), both the size and the position are more consistent with the image. Figure 8(c) shows the trajectories from both methods (red for original HT, yellow for corrected). Two improvements are immediately noticed: (i) the corrected trajectory is generally higher, closer to the actual center of the droplet; (ii) the “lat-

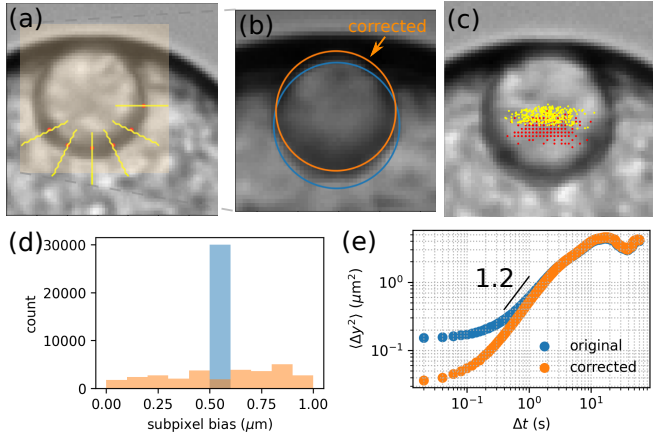


FIG. 8. A custom method to improve tracking accuracy of HT method. (a) Illustration of cross-boundary intensity profiles. (b) Original detection (blue) and corrected detection (orange). (c) Original trajectory (red) and corrected trajectory (yellow). (d) Subpixel bias of original trajectory (blue) and improved trajectory (orange). (e) MSD of original trajectory (blue) and improved trajectory (orange).

tice” like pattern in the original trajectory is absent in corrected trajectory, suggesting less subpixel bias. Indeed, the subpixel statistics is shown in Fig. 8, and we see considerable improvement on the subpixel bias. We compared the MSD of both trajectories, as shown in Fig. 8(e). At short times, the corrected MSD is generally smaller, while at long times, the two MSD are indistinguishable. This difference is expected: HT does not detect droplet location accurately. At each step, it adds uncertainty to the detected location, making the short time displacement artificially larger. At long times, however, this artificial displacement becomes less important compared to the actual displacement, so that the two MSD converge. Interestingly, both MSD exhibit subdiffusive regimes at short times, suggesting that even the corrected trajectory is subject to detection noise. It is challenging to eliminate detection noise by further correction of the trajectories. Therefore, we acknowledge the presence of this noise and incorporate it in our model to fit experimental MSD. The results are satisfactory.

Appendix B: Image analysis

Videos are shot between 30-70 fps, with the majority shot at 50 fps for 10 minutes, therefore, to extract the position of the outer and inner droplet we have to analyze about 30000 images. To do that, we made a tracking script in Matlab that detects both droplets using a Matlab function called *imfindcircles*. This function finds circles of given radius range and with certain contrast. So we can find dark circles or bright circles of given radii, more parameters can be added to the function, such as sensitivity. The steps to perform the detection of the

droplets are summarized in the figure (9). The steps to track the droplets are: The initial image is cropped to make detection less resource-intensive, the Matlab *Drawcircle* function is used on this image to compute the diameter and center of the outer and inner droplet. From the center and radii of the inner droplet we make a template of the inner droplet with a size of 1.2 times the inner radii. Now we perform some image adjustments to increase the contrast and make the detection easier. Then using the function *imfindcircles* for the inner droplet and the outer droplet. For the inner droplet we give to the function a parameter of the radius $r_i \pm \delta$, where δ is a constant times the radius detected in the image $k - 1$. We are detecting the inner droplet in the template image, in the step k the template image is compared with the image in the step $k - 1$ using the crosscorrelation function *corr2*. This function gives a value between [0 – 1], if this value is 1 then the image is identical to the image in the step before. We put the condition if this value is less than 0.5 then increase the value of δ and so on. The function *imfindcircles* will detect in a range of radius, so in two consecutive image this value of radius can change and therefore change the center of the inner droplet in a small quantity.

After detection, on the raw data the data can be smoothed to remove small fluctuations, but the question now arises, how much can we smooth so as not to remove information about the internal droplet motion?.

Appendix C: Smoothdata analysis

We want to study how data smoothing through affects the measured observables. The *smoothdata* function is the function included in the Matlab toolbox, which, as shown in the figure 10 the unanalyzed position shows large variations that as the window size increases for the *smoothdata* function decrease. The *smoothdata* function returns a moving average of the elements of the position vector determined by one. In the data we have used the Gaussian method which weights the window with a Gaussian weight. The *smoothn* function provides a dis-

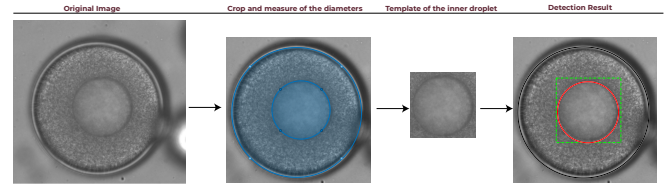
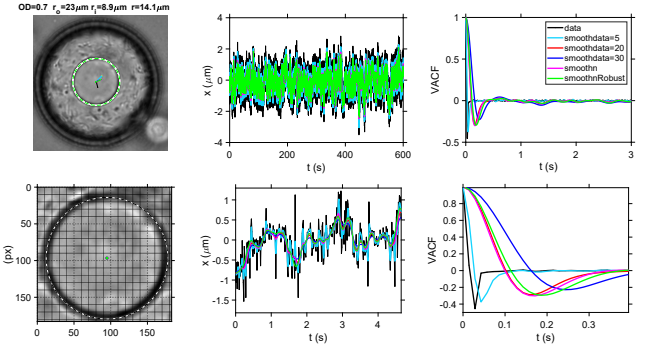


FIG. 9. Tracking. - From left to right: The initial image is cropped. Then draw two circles to calculate the diameters of the drops. An inner droplet template is created with a size of 1.2 times the radii of the inner droplet. Then we detect the outer drop using *imfindcircles* over the cropped image and the same over the template of the inner droplet.

crete, robust, unsupervised and fast smoothing method for arbitrary-dimensional data of arbitrary dimension.



The videos will show the result of the detection of the internal droplet, the difference of the position between two positions $\Delta X = X_{n+1} - X_n$, the X and Y position in time where the time axis moves with the data and a cropping of the internal droplet in time where the image axes remain fixed according to the position of the center of the internal droplet in the initial image plus 1.1 times its radius. (see videos frame by frame)

Appendix D: MSD computation

$$\dot{x} = u(t) - \frac{1}{\tilde{\tau}}x, \quad (D1)$$

We can solve this using the Laplace transform, then $x(t)$ is:

$$x(t) = x_0 e^{-\frac{1}{\tilde{\tau}}t} + \int_0^t e^{-\frac{1}{\tilde{\tau}}(t-s)} u(s) ds, \quad (D2)$$

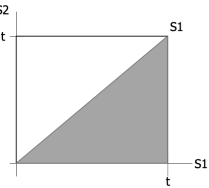
We will assume that the noise autocorrelation is of the form $\langle u(t)u(t') \rangle = v_b^2 e^{-|t-t'|/\tau}$, where v_b^2 is the noise amplitude and τ is the persistence time. Also, we will assume that the initial position is independent of the noise, $\langle x(0)u(t) \rangle = 0$. Having this we can compute the mean square displacement (MSD) as:

$$\langle \Delta x^2 \rangle = 2e^{-\frac{1}{\tilde{\tau}}t} \int_0^t ds e^{-\frac{1}{\tilde{\tau}}(t-s)} \langle x(0)u(t) \rangle + \int_0^t \int_0^t ds_1 ds_2 e^{-\frac{1}{\tilde{\tau}}(t-s_1)} e^{-\frac{1}{\tilde{\tau}}(t-s_2)} u(s_1)u(s_2) \quad (D3)$$

$$\langle \Delta x^2 \rangle = \int_0^t \int_0^t ds_1 ds_2 e^{-\frac{1}{\tilde{\tau}}(t-s_1)} e^{-\frac{1}{\tilde{\tau}}(t-s_2)} u(s_1)u(s_2) ds_1 ds_2 \quad (D4)$$

$$\langle \Delta x^2 \rangle = \int_0^t \int_0^t ds_1 ds_2 e^{-\frac{1}{\tilde{\tau}}(t-s_1)} e^{-\frac{1}{\tilde{\tau}}(t-s_2)} e^{-|s_1-s_2|/\tau}, \quad (D5)$$

for the integration, we will use:



and the integral change as $\int_0^t ds_1 \int_0^t ds_2 = 2 \int_0^t ds_1 \int_0^{s_1} ds_2$, with $s_1 > s_2$ and then $e^{-|s_1-s_2|/\tau} = e^{-(s_1-s_2)/\tau}$. we have:

$$\langle \Delta x^2 \rangle = \int_0^t ds_1 \int_0^{s_1} ds_2 e^{-\frac{1}{\tilde{\tau}}(t-s_1)} e^{-\frac{1}{\tilde{\tau}}(t-s_2)} e^{-(s_1-s_2)\frac{1}{\tau}}, \quad (D6)$$

After the integration, the MSD is:

$$\langle \Delta x^2 \rangle = \frac{2v_b^2}{\left(\frac{1}{\tilde{\tau}} + \frac{1}{\tau}\right)} \left[\frac{1}{2\frac{1}{\tilde{\tau}}} (1 - e^{-2\frac{1}{\tilde{\tau}}t}) - \frac{1}{\frac{1}{\tilde{\tau}} - \frac{1}{\tau}} (e^{-(\frac{1}{\tilde{\tau}} + \frac{1}{\tau})t} - e^{-2\frac{1}{\tilde{\tau}}t}) \right], \quad (\text{D7})$$

Expanding the equation to study the limits cases.

$$= \frac{v_b^2}{\frac{1}{\tilde{\tau}}\left(\frac{1}{\tilde{\tau}} + \frac{1}{\tau}\right)} - \frac{v_b^2 e^{-2\frac{1}{\tilde{\tau}}t}}{\frac{1}{\tilde{\tau}}\left(\frac{1}{\tilde{\tau}} + \frac{1}{\tau}\right)} + \frac{2v_b^2 e^{-2\frac{1}{\tilde{\tau}}t}}{\left(\frac{1}{\tilde{\tau}} - \frac{1}{\tau}\right)\left(\frac{1}{\tilde{\tau}} + \frac{1}{\tau}\right)} - \frac{2v_b^2 e^{-(\frac{1}{\tilde{\tau}} + \frac{1}{\tau})t}}{\left(\frac{1}{\tilde{\tau}} - \frac{1}{\tau}\right)\left(\frac{1}{\tilde{\tau}} + \frac{1}{\tau}\right)} \quad (\text{D8})$$

Now we can study the limits cases as: For short's times $t \rightarrow 0$:

$$\langle \Delta x^2 \rangle \approx v_b^2 t^2. \quad (\text{D9})$$

For $t \rightarrow \infty$:

$$\langle \Delta x^2 \rangle \approx \frac{v_b^2}{\frac{1}{\tilde{\tau}}\left(\frac{1}{\tilde{\tau}} + \frac{1}{\tau}\right)}. \quad (\text{D10})$$

We can see that for short times, the MSD has a ballistic behavior, and for long times the MSD saturates. We will compute the velocity autocorrelation $C(t, t') = \langle v(t)v(t') \rangle$ using the equation D1 with an initial condition in the infinity. The solution of the equation with this initial condition is:

$$x(t) = \int_{-\infty}^t e^{-\frac{1}{\tilde{\tau}}(t-s)} u(s) ds. \quad (\text{D11})$$

The velocity autocorrelation function is:

$$C(t, t') = \langle v(t)v(t') \rangle = \left\langle \left(u(t) - \frac{1}{\tilde{\tau}}x(t) \right) \left(u(t') - \frac{1}{\tilde{\tau}}x(t') \right) \right\rangle, \quad (\text{D12})$$

$$C(t, t') = \langle u(t)u(t') \rangle - \frac{1}{\tilde{\tau}} \langle u(t)x(t') \rangle - \frac{1}{\tilde{\tau}} \langle x(t)u(t') \rangle + \frac{1}{\tilde{\tau}^2} \langle x(t)x(t') \rangle. \quad (\text{D13})$$

The first term is the noise autocorrelation $\langle u(t)u(t') \rangle = v_b^2 e^{-\frac{1}{\tilde{\tau}}|t-t'|}$. To solve the integrals, we will assume that $t > t'$.

The integral $\langle x(t)u(t') \rangle$:

$$\langle x(t)u(t') \rangle = v_b^2 \int_{-\infty}^t ds e^{-\frac{1}{\tilde{\tau}}(t-s)} e^{-\frac{1}{\tilde{\tau}}|t'-s|}, \quad t > t' \quad (\text{D14})$$

$$= v_b^2 \int_{-\infty}^{t'} ds e^{-\frac{1}{\tilde{\tau}}(t-s)-\frac{1}{\tilde{\tau}}(t'-s)} + v_b^2 \int_{t'}^t ds e^{-\frac{1}{\tilde{\tau}}(t-s)-\frac{1}{\tilde{\tau}}(s-t')}, \quad (\text{D15})$$

$$= \frac{v_b^2 e^{-\frac{1}{\tilde{\tau}}(t-t')}}{\frac{1}{\tilde{\tau}} + \frac{1}{\tau}} + \frac{v_b^2 e^{-\frac{1}{\tilde{\tau}}(t-t')} - v_b^2 e^{-\frac{1}{\tilde{\tau}}(t-t')}}{\frac{1}{\tilde{\tau}} - \frac{1}{\tau}}. \quad (\text{D16})$$

The second term integral is:

$$\langle u(t)x(t') \rangle = \int_{-\infty}^{t'} ds e^{-\frac{1}{\tilde{\tau}}(t'-s)} e^{-\frac{1}{\tilde{\tau}}(t-s)}, \quad (\text{D17})$$

$$= \frac{e^{-\frac{1}{\tilde{\tau}}(t-t')}}{\frac{1}{\tilde{\tau}} + \frac{1}{\tau}}. \quad (\text{D18})$$

And the last integral:

$$\langle x(t)x(t') \rangle = \int_{-\infty}^t ds \int_{-\infty}^{t'} ds' e^{-\frac{1}{\tilde{\tau}}(t-s)} e^{-\frac{1}{\tilde{\tau}}(t'-s')} e^{-\frac{1}{\tilde{\tau}}|s-s'|}, \quad (\text{D19})$$

$$(D20)$$

Where we will use the same procedure as before to change the limits of integration. We have first:

$$C_I = \int_{-\infty}^{t'} ds \int_{-\infty}^{t'} ds' e^{-\frac{1}{\tilde{\tau}}(t-s)} e^{-\frac{1}{\tilde{\tau}}(t'-s')} e^{-\frac{1}{\tau}(s'-s)}, \quad (\text{D21})$$

$$= \int_{-\infty}^{t'} ds \int_s^{t'} ds' e^{(\frac{1}{\tilde{\tau}} + \frac{1}{\tau})s} e^{(\frac{1}{\tilde{\tau}} - \frac{1}{\tau})s'} e^{-\frac{1}{\tilde{\tau}}t} e^{-\frac{1}{\tilde{\tau}}t'}, \quad (\text{D22})$$

$$= \frac{1}{\frac{1}{\tilde{\tau}} - \frac{1}{\tau}} \int_{-\infty}^{t'} ds \left[e^{(\frac{1}{\tilde{\tau}} - \frac{1}{\tau})t'} e^{(\frac{1}{\tilde{\tau}} + \frac{1}{\tau})s} - e^{2\frac{1}{\tilde{\tau}}s} \right], \quad (\text{D23})$$

$$= \frac{e^{-\frac{1}{\tilde{\tau}}(t-t')}}{\frac{1}{\tilde{\tau}} - \frac{1}{\tau}} \left(\frac{1}{\frac{1}{\tilde{\tau}} + \frac{1}{\tau}} - \frac{1}{2\frac{1}{\tilde{\tau}}} \right). \quad (\text{D24})$$

The next part of the integral is:

$$C_{II} = \int_{-\infty}^{t'} ds' \int_{s'}^t ds e^{-\frac{1}{\tilde{\tau}}(t-s)} e^{-\frac{1}{\tilde{\tau}}(t'-s')} e^{-\frac{1}{\tau}(s-s')}, \quad (\text{D25})$$

$$= e^{-\frac{1}{\tilde{\tau}}t - \frac{1}{\tilde{\tau}}t'} \int_{-\infty}^{t'} ds' \int_{s'}^t ds e^{(\frac{1}{\tilde{\tau}} - \frac{1}{\tau})s} e^{(\frac{1}{\tilde{\tau}} + \frac{1}{\tau})s'}, \quad (\text{D26})$$

$$= \frac{e^{-\frac{1}{\tilde{\tau}}t - \frac{1}{\tilde{\tau}}t'}}{\frac{1}{\tilde{\tau}} - \frac{1}{\tau}} \int_{-\infty}^{t'} ds' \left[e^{(\frac{1}{\tilde{\tau}} - \frac{1}{\tau})t} e^{(\frac{1}{\tilde{\tau}} + \frac{1}{\tau})s'} - e^{\frac{2}{\tilde{\tau}}s'} \right], \quad (\text{D27})$$

$$= \frac{1}{(\frac{1}{\tilde{\tau}} - \frac{1}{\tau})(\frac{1}{\tilde{\tau}} + \frac{1}{\tau})} e^{-\frac{1}{\tilde{\tau}}(t-t')} - \frac{1}{2(\frac{1}{\tilde{\tau}} - \frac{1}{\tau})} e^{-\frac{1}{\tilde{\tau}}(t-t')}. \quad (\text{D28})$$

Bringing together all the terms, the velocity autocorrelation function is:

$$C(t, t') = \frac{v_b^2}{(\frac{1}{\tilde{\tau}} + \frac{1}{\tau})(\frac{1}{\tilde{\tau}} - \frac{1}{\tau})} \left[\left(\frac{1}{\tilde{\tau}^2} + \frac{\frac{1}{\tilde{\tau}}}{\tau} - \frac{1}{\tau^2} \right) e^{-\frac{1}{\tilde{\tau}}(t-t')} - \frac{1}{\tilde{\tau}^2} e^{-\frac{1}{\tilde{\tau}}(t-t')} \right], \quad t > t' \quad (\text{D29})$$

For $t = t'$

$$C(t, t) = \langle v^2 \rangle = \frac{v_b^2}{\frac{1}{\tilde{\tau}}\tau + 1} = \frac{v_b^2 \tilde{\tau}}{\tau + \tilde{\tau}}, \quad (\text{D30})$$

- [1] H. Kurtuldu, J. S. Guasto, K. A. Johnson, and J. P. Gollub, Enhancement of biomixing by swimming algal cells in two-dimensional films, *Proceedings of the National Academy of Sciences* **108**, 10391 (2011).
- [2] D. O. Pushkin and J. M. Yeomans, Fluid Mixing by Curved Trajectories of Microswimmers, *Physical Review Letters* **111**, 188101 (2013).
- [3] D. Saintillan and M. J. Shelley, Instabilities, pattern formation, and mixing in active suspensions, *Physics of Fluids* **20**, 123304 (2008).
- [4] A. Sokolov, R. E. Goldstein, F. I. Feldchtein, and I. S. Aranson, Enhanced mixing and spatial instability in concentrated bacterial suspensions, *Physical Review E* **80**, 031903 (2009).
- [5] J. Dunkel, V. B. Putz, I. M. Zaid, and J. M. Yeomans, Swimmer-tracer scattering at low Reynolds number, *Soft Matter* **6**, 4268 (2010).
- [6] J. R. Blake and A. T. Chwang, Fundamental singularities of viscous flow, *Journal of Engineering Mathematics* **8**, 23 (1974).
- [7] G. Miño, T. E. Mallouk, T. Darnige, M. Hoyos, J. Dauchet, J. Dunstan, R. Soto, Y. Wang, A. Rousselet, and E. Clément, Enhanced diffusion due to active swimmers at a solid surface, *Physical Review Letters* **106**, 10.1103/physrevlett.106.048102 (2011).
- [8] G. L. Miño, J. Dunstan, A. Rousselet, E. Clément, and R. Soto, Induced diffusion of tracers in a bacterial suspension: theory and experiments, *Journal of Fluid Mechanics* **729**, 423 (2013).
- [9] A. Lagarde, N. Dagès, T. Nemoto, V. Démery, D. Bartolo, and T. Gibaud, Colloidal transport in bacteria suspensions: From bacteria scattering to anomalous and enhanced diffusion, *Soft Matter* **16**, 7503 (2020), arXiv:2002.10144.
- [10] G. Grégoire, H. Chaté, and Y. Tu, Active and passive particles: Modeling beads in a bacterial bath, *Physical Review E* **64**, 011902 (2001).

- [11] C. Maggi, M. Paoluzzi, N. Pellicciotta, A. Lepore, L. Angelani, and R. Di Leonardo, Generalized Energy Equipartition in Harmonic Oscillators Driven by Active Baths, *Physical Review Letters* **113**, 238303 (2014).
- [12] X.-L. Wu and A. Libchaber, Particle Diffusion in a Quasi-Two-Dimensional Bacterial Bath, *Physical Review Letters* **84**, 3017 (2000).
- [13] S. Ye, P. Liu, F. Ye, K. Chen, and M. Yang, Active noise experienced by a passive particle trapped in an active bath, *Soft Matter* **16**, 4655 (2020).
- [14] H. Wioland, F. G. Woodhouse, J. Dunkel, J. O. Kessler, and R. E. Goldstein, Confinement Stabilizes a Bacterial Suspension into a Spiral Vortex, *Physical Review Letters* **110**, 268102 (2013).
- [15] K.-T. Wu, J. B. Hishamunda, D. T. N. Chen, S. J. DeCamp, Y.-W. Chang, A. Fernández-Nieves, S. Fraden, and Z. Dogic, Transition from turbulent to coherent flows in confined three-dimensional active fluids, *Science* **355**, eaal1979 (2017).
- [16] Z. Liu, K. Zhang, and X. Cheng, Rheology of bacterial suspensions under confinement, *Rheologica Acta* **58**, 439 (2019).
- [17] J. E. Keymer, P. Galajda, G. Lambert, D. Liao, and R. H. Austin, Computation of mutual fitness by competing bacteria, *Proceedings of the National Academy of Sciences* **105**, 20269 (2008).
- [18] T. Minamino, Y. Imae, F. Oosawa, Y. Kobayashi, and K. Oosawa, Effect of intracellular pH on rotational speed of bacterial flagellar motors, *Journal of Bacteriology* **185**, 1190 (2003).
- [19] G. Ramos, M. L. Cordero, and R. Soto, Bacteria driving droplets, *Soft Matter* **16**, 1359 (2020).
- [20] G. Stockman and L. G. Shapiro, *Computer Vision* (Pearson, Upper Saddle River, NJ, 2001).
- [21] A. Liberzon, T. Käufer, A. Bauer, P. Vennemann, and E. Zimmer, OpenPiv (2021).
- [22] K. C. Leptos, J. S. Guasto, J. P. Gollub, A. I. Pesci, and R. E. Goldstein, Dynamics of Enhanced Tracer Diffusion in Suspensions of Swimming Eukaryotic Microorganisms, *Physical Review Letters* **103**, 198103 (2009).
- [23] A. E. Hamby, D. K. Vig, S. Safanova, and C. W. Wolgemuth, Swimming bacteria power microspin cycles, *Science Advances* **4**, eaau0125 (2018).
- [24] E. Lushi, H. Wioland, and R. E. Goldstein, Fluid flows created by swimming bacteria drive self-organization in confined suspensions, *Proceedings of the National Academy of Sciences* **111**, 9733 (2014).
- [25] M. Rajabi, H. Baza, T. Turiv, and O. D. Lavrentovich, Directional self-locomotion of active droplets enabled by nematic environment, *Nature Physics* **17**, 260 (2021).
- [26] B. Vincenti, G. Ramos, M. L. Cordero, C. Douarche, R. Soto, and E. Clement, Magnetotactic bacteria in a droplet self-assemble into a rotary motor, *Nature Communications* **10**, 5082 (2019).
- [27] H. C. Berg, *E. Coli in Motion*, Biological and Medical Physics Series (Springer, New York, 2004).